CrossMark

# Hydrothermal Synthesis of CNTs/Co$_3$O$_4$@rGO Mesopours Nanocomposite as a Room Temperature Gas Sensor for VOCs

M. Morsy$^1$ · I. S. Yahia$^{2,3}$ · H. Y. Zahran$^{2,3}$ · M. Ibrahim$^4$

## Abstract

In the present paper, the effect of reduced graphene oxide (rGO) and carbon nanotubes (CNTs) on the gas-sensing properties of Co$_3$O$_4$ has been reported. The Co$_3$O$_4$/CNTs@rGO composite was synthesized using hydrothermal method. Samples were characterized by high resolution transmission electron microscope, Raman spectroscopy, Fourier transform infrared spectroscopy, differential thermal analysis, thermogravimetric analysis, Brunauer–Emmett–Teller surface area, and Barrett–Joyner–Halenda pore size measurements. The X-ray diffraction measurements confirmed the formation of the Co$_3$O$_4$ spinel structure. The Co$_3$O$_4$/CNTs@rGO exhibited mesoporous structure and high specific surface area of 92.9 m$^2$/g. The gas-sensing properties of the synthesized composite are evaluated toward volatile organic compounds (VOCs). The gas-sensing tests revealed that the prepared composite showed a remarkable response to ethanol at room temperature compared to other volatile organic compounds with fast response time. Due to the intriguing merits characteristics, Co$_3$O$_4$/CNTs@rGO composite could achieve remarkable sensitivity to VOCs especially ethanol, demonstrating great potential in next-generation room-temperature gas sensor based on P-type semiconductor.

**Keywords** Gas sensors · Volatile organic compounds · rGO · CNTs and thermal analysis

## 1 Introduction

Gas sensors are widely utilized in everyday life events including environmental pollutants monitoring, home security, public health, and automotive gas emission [1–4]. The detection of harmful gases and particularly VOCs is becoming a great challenge [5]; accordingly the new technologies must be utilized to develop fast response, selective and room-temperature operated gas sensors. Many trials were made to enhance the sensitivity of gas sensors which is a critical parameter to satisfy the needs of detection of toxic and harmful gases [6]. Recent research and development in nanotechnology enabled scientists to implement Co$_3$O$_4$ nanostructure in various applications [7] including Li-ion battery [8], super capacitor [9, 10], catalytic oxidation, and seawater splitting electrode [11].

Currently a great attention is directed toward n-type semiconductor, while the gas-sensing properties of the p-type semiconductors acquired little attention in gas sensor applications, [12]. Among different p-types of semiconductor materials, nano-structured Co$_3$O$_4$ with different morphologies have been tested as VOCs sensor due to its high catalytic activity and low fabrication cost [13–16], nevertheless the optimum working temperature still relatively high. The sensing mechanisms of metal oxide gas sensors rely on the adsorption/desorption processes which mainly occur on the outer layer and determine the response of the sensors. Since the sensitivity of the sensor depends on the shape, size and surface area, therefore 1-dimensional nano-structured materials with high aspect ratio are promising candidates for gas sensor applications [17, 18]. Nanomaterials

✉ M. Morsy
83morsy@gmail.com

$^1$ Building Physics and Environment Institute, Housing & Building National Research Center (HBRC), Dokki, 12311 Giza, Egypt

$^2$ Advanced Functional Materials & Optoelectronic Laboratory (AFMOL), Physics Department, Faculty of Science, King Khalid University, Abha, Saudi Arabia

$^3$ Nanoscience Laboratory for Environmental and Biomedical Applications (NLEBA), Semiconductor Laboratory, Metallurgical Laboratory 2 Physics Department, Faculty of Education, Ain Shams University, Roxy, 11757 Cairo, Egypt

$^4$ Spectroscopy Department, National Research Centre, 33 El-Bohouth Str., Dokki, 12622 Giza, Egypt

and especially carbon nanomaterials (graphene and carbon nanotubes) possess amazing properties that enable them to be marvelous candidates for sensing applications especially when alloyed with other metal oxide semiconductor [19, 20]. Carbon-based materials can form nanocomposites for several applications; the most recent of them are for sensing properties owing to their unique surface properties [21]. Significant efforts have been devoted to utilize $Co_3O_4$/graphene nanocomposite for energy storage applications like supercapacitor and Li-ion battery [22, 23]; however, little attention focused on gas sensor application.

The gas-sensing mechanism of the $Co_3O_4$ nanostructures was studied related to its microstructural factors such as specific surface area and pore size. $Co_3O_4$ and its compounds have porous form and modified surfaces that are important in adsorption and desorption processes encourage its applications in the field of gas sensors [3, 24].

To get a novel structure with enhanced sensitivity, $Co_3O_4$ alloyed with rGO and CNTs was synthesized using hydrothermal method. In light of the above considerations, the present work aims to reduce the working temperature of $Co_3O_4$ and evaluates its response toward VOCs. Characterizations like X-ray diffraction (XRD), Fourier transform infrared (FTIR), Raman, high resolution transmission electron microscope (HRTEM) and thermal analysis were used in this study to prove the successful synthesis of rGO/CNTs/$Co_3O_4$ nanocomposite.

## 2 Experimental

Cobalt nitrate hexahydrate was purchased from Alpha Chemka, Urea was obtained from El-Nasr pharmaceutical Co. Ammonium fluoride was purchased from Lobal Chemie. All chemicals were used as it is without any purification or treatment. CNTs synthesized by floating-catalyst chemical vapor deposition method and functionalized with COOH group. GO was synthesized by modified Hummer method. All details concerning MWCNTs and GO synthesizing were reported in our previous work [25, 26]. 2.91 g of $Co(NO_3)6H_2O$ was dissolved in 50 ml distilled water for 10 min using magnetic stirrer, subsequently 1.92 g of ammonium fluoride was slowly added over 10 min. 75 mg of GO and 75 mg of MWCNTs was suspended in 50 ml $H_2O$ using ultrasonic waves for 30 min. The above two solutions were mixed for 2 h and aged for 24 h at room temperature. 5 g of urea in 20 ml $H_2O$ was added drop wise to the mixture over 1 h. The overall resultant solution was transferred to 100 ml autoclave and kept at 120 °C for 24 h. The black precipitates were collected by filtration, washed several times and dried in air at 60 °C for 12 h. Finally, the black $Co_3O_4$ CNTs@rGO was obtained by calcination of the as-prepared precipitates at 300 °C for 1 h in air as shown in Fig. 1. The calcination temperature was decided based on thermogravimetric analysis (TGA) measurement data.

## 3 Characterization Techniques

- The microstructures were examined by a HRTEM (FEI Tecnai G2 F20) operated at 200 kV.
- The crystal structure was identified using Philips XRD diffractometer (PW3050/60) with Cu Kα radiation ($\lambda = 0.15406$ nm).
- Raman spectra was collected by (SENTERRA—Bruker, Germany) instrument with laser source (Nd:YAG) at wavelength 532 nm.
- The molecular structure was investigated by FTIR spectrophotometer Vertex 70, Bruker Optik, Germany.
- Thermal analysis including differential thermal analysis (DTA) and TGA was measured via STD Q-600 thermal analyzer under air atmosphere in the temperature range from room temperature (RT) up to 800 °C.



**Fig. 1** Schematic representation of preparation process
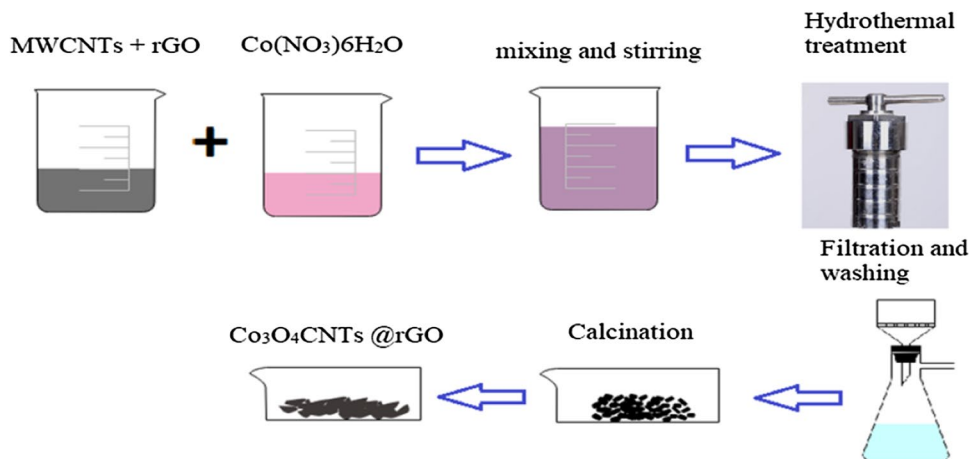
- Brunauer–Emmett–Teller (BET) surface area and Barrett–Joyner–Halenda (BJH) pore diameter distribution were conducted using Quantachrome NOVA analyzer instrument.

## 4 Results and Discussions

HRTEM was utilized to confirm the morphology of the resultant composite as shown in Fig. 2a, b, c. The HRTEM observations demonstrated that the resultant composite contains semispherical $Co_3O_4$ particles attached to both the CNTs and the rGO surfaces. The rGO sheets are densely covered by $Co_3O_4$ nanoparticles, while the CNTs are partially loaded with $Co_3O_4$. The HRTEM image of Fig. 2a indicates that the crystalline semisphere of $Co_3O_4$ with an average size of about 9–15 nm covers the outer surface of the CNTs and the rGO. The selected area electron diffraction (SAED) pattern of $Co_3O_4$ nanoparticles is shown in Fig. 2d. The bright spots on concentric circles in the SAED confirmed the crystalline nature of $Co_3O_4$ nanoparticles.

XRD analysis was performed for the resultant phase identification as shown in Fig. 3. The diffraction peak at 25.29°, corresponds to (002) crystal planes of graphite, indicating the presence of rGO and CNTs. The interplanar spacing corresponding to the (002) peak of rGO (0.368 nm) is larger than that of standard graphite (0.335 nm) giving confirmation that oxygen-containing functional groups had been generated, providing additional intercalation sites for adsorption of gas molecules and therefore promoting enhanced gas sensing performance [27].

The diffraction peaks at 31.3, 36.7, 44.8, 59.1, 65.1° can be indexed to (220), (311), (400), (511) and (440) (JCPDS No. 43-1003) indicating the formation of $Co_3O_4$ [28–30]. No other diffraction peaks belonging to any impurities were observed, indicating high purity of the composites.
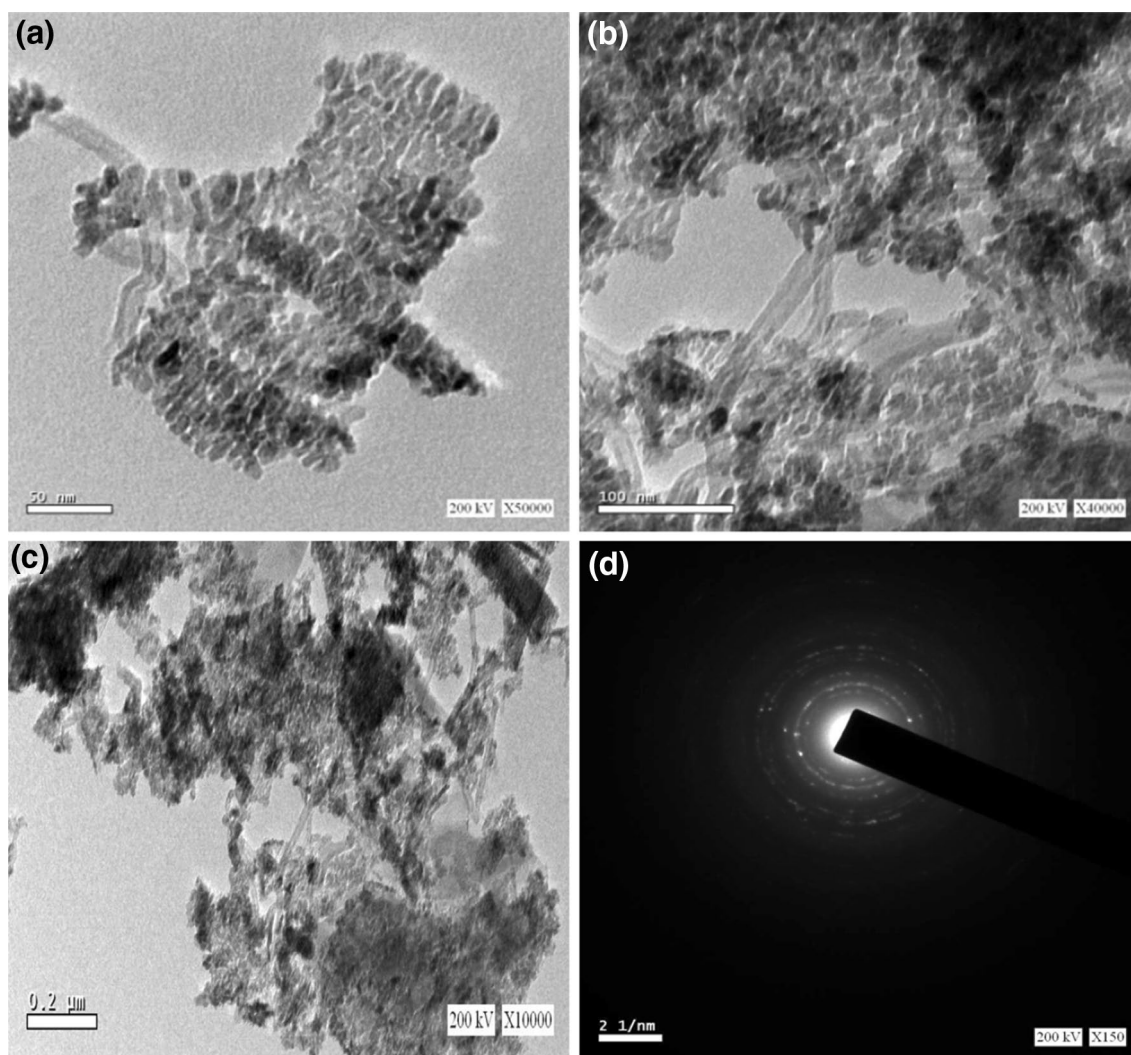


**Fig. 2** **a, b, c** The HRTEM of $Co_3O_4$/CNTs@rGO composite and **d** the SAED of $Co_3O_4$ nanoparticles

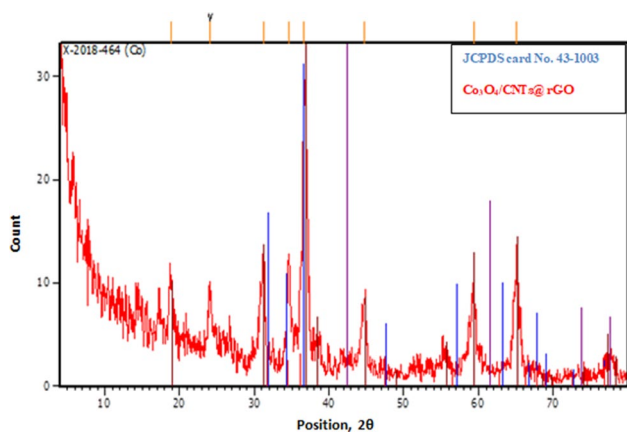**Fig. 3** XRD of Co$_3$O$_4$/CNTs@rGO composite

Spectroscopic techniques including Raman and FTIR were used to ensure the crystal structure of the prepared composites. The structure of Co$_3$O$_4$ with Co$^{2+}$ (3d$^7$) and Co$^{3+}$ (3d$^6$) located at tetrahedral and octahedral sites, respectively, belongs to the space group (Fd3m). The group theory predicts the following modes in the spinel structure:

$$\Gamma = A_{1g}(R) + E_g(R) + F_{1g}(in) + 3F_{2g}(R) + 2A_{2u}(in) + 2Eu\,(in) + 4F_{1u}(IR) + 2F_{2u}(in),$$

where (R), (IR) and (in) represent Raman active vibrations, infrared-active vibration and inactive modes, respectively.

The Raman spectra of the Co$_3$O$_4$/CNTs@rGO composite are shown in Fig. 4, in which the G$^\backslash$, G and D peaks were observed at 2680 cm$^{-1}$, 1568 cm$^{-1}$ and 1340 cm$^{-1}$, which are associated with second-order process activated
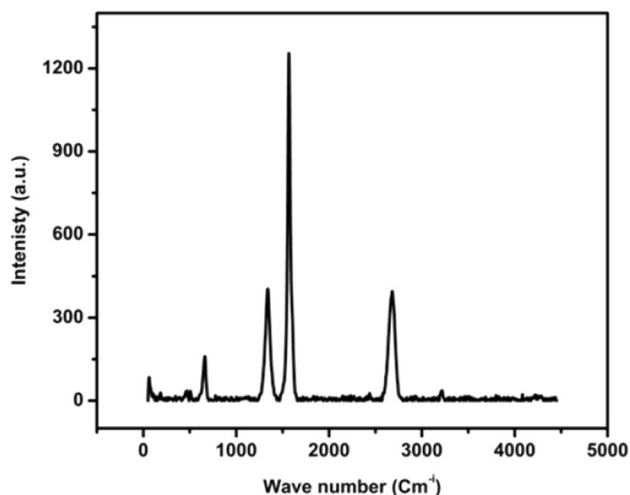
by double resonance (DR) processes, sp2 hybridization of carbon atoms and disorder due to the defects induced on the sp2 hybridized sheet, respectively [23, 31, 32]. The Raman shifts at 663, 505, and 469 cm$^{-1}$ correspond to A1g, F2g, and Eg vibration modes of Co$_3$O$_4$ respectively [30].

The FTIR spectra of Co$_3$O$_4$/CNTs@rGO are shown in Fig. 5 in the investigated region (4000–400 cm$^{-1}$). The obtained spectra manifested the presence of two bands at 566 cm$^{-1}$ and 662 cm$^{-1}$, corresponding to vibrations in the Co$^{3+}$ and stretching vibrations in the Co$^{2+}$ which confirm the formation of Co$_3$O$_4$ spinel oxide. In addition to Co$_3$O$_4$ bands, FTIR also exhibits several characteristic bands of oxygen-containing groups. The band at 2361 cm$^{-1}$ can be associated with the O–H stretch from strongly hydrogen-bonded –COOH.

The band at 1558 cm$^{-1}$ is related to the carboxylate anion stretch mode [33]. The band at 1340 cm$^{-1}$ could be ascribed to C=O stretching vibrations [34]. It can be seen that the spectrum retains a broad band centered at 3400 cm$^{-1}$, which is attributed to the residual O–H groups of rGO. These results confirmed the existence of CNTs, rGO as well as crystalized Co$_3$O$_4$ nanoparticles as confirmed by HRTEM and XRD measurements.

Thermal analysis in terms of DTA and TGA shown in Fig. 6 was conducted from RT up to 800 °C under air atmosphere. For DTA measurement, one exothermic peak ranging from 427 to 537 °C with peak value at 500 °C could be attributed to the consumption of rGO and CNTs. It was observed that the oxidation temperature of CNTs shifted to



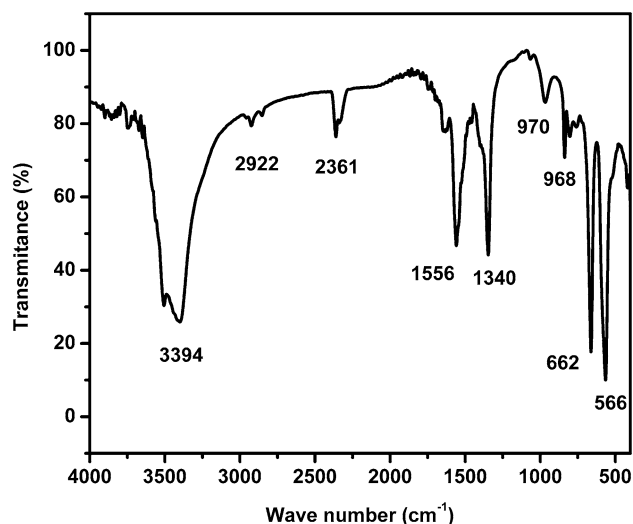**Fig. 4** Raman spectrum of Co$_3$O$_4$/CNTs@rGO composite



**Fig. 5** FTIR spectrum of Co$_3$O$_4$/CNTs@rGO composite
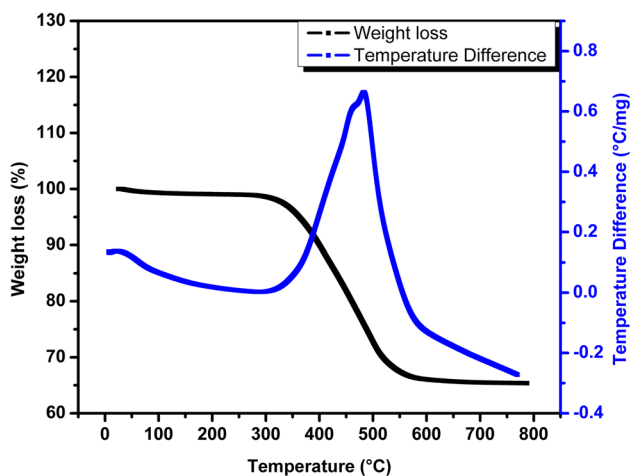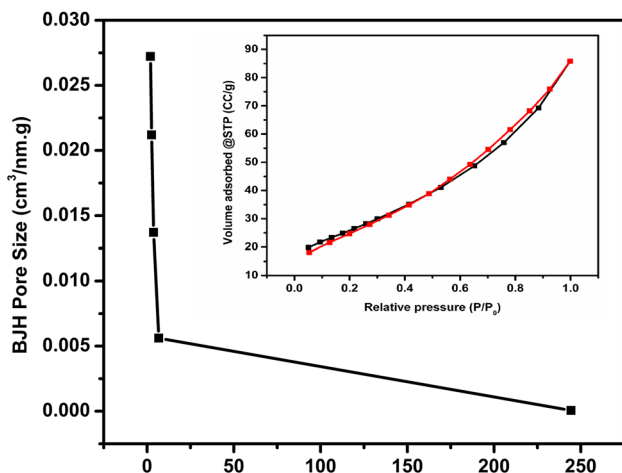
**Fig. 6** TGA and DTA thermogram of $Co_3O_4$/CNTs@rGO



**Fig. 7** BET and BJH of $Co_3O_4$/CNTs@rGO

lower value, and this could be due to the initial temperature of the oxidative process of CNTs directly related to the presence of lattice defects arising from hydrothermal treatment; the less the defects, the higher the decomposition temperature [25]. The mass ratio of $Co_3O_4$ loaded on CNTs/rGO was estimated based on TGA measurement to be 34 wt%.

The specific surface area and pore size of $Co_3O_4$/CNTs@rGO composite estimation using the $N_2$ adsorption–desorption measurements was performed at a relative pressure of 0.1–1.0 as depicted in Fig. 7. It was observed that according to IUPAC classification, the composite displayed type III isotherm with H3 adsorption hysteresis loop. The specific surface area of the $Co_3O_4$/CNTs@rGO composite was calculated by BET method to be 92.88 $m^2/g$ while the corresponding BJH pore-size was estimated by BJH to be 2 nm indicating the presence of a mesoporous structure [12, 35]. The mesoporous structures have been reported to show very

high gas responses and rapid gas responding kinetics, which are attributed to their high surface area and well-defined porous architecture, respectively [36].

## 4.1 Sensing Response

200 mg of the $Co_3O_4$ CNTs@rGO composite was suspended in 1 ml of distilled water and grounded in agate mortar for 5 min in order to form a homogeneous past. Two copper wires were attached to the surface of the FTO substrate via two copper foils coated with conductive adhesive. A proper amount of the composite was applied onto an FTO substrate and conditioned at 80 °C for 4 h. The fabricated sensor was aged at 5V for 36 h before evolution to enhance its stability. The concentrations of VOCs were estimated based on the following formula:

$$Vi = \frac{CVMW}{22.45D} \qquad (1)$$

where MW is the molecular weight of ethanol, D is the density, V is the chamber volume, and C is the concentration in ppm, The gas-sensing experiments were conducted by exposing the $Co_3O_4$ CNTs@rGO sensor to various concentrations of VOC gas.

The electrical resistance variation of the sensor are automatically recorded using Keithley 6485 Picoammeter connected to a computer via RS-232 interface. The normalized response (S) of the sensor is determined by

$$S = \frac{(R_g - R_0)}{R_0} \times 100 \qquad (2)$$

where $R_g$ and $R_0$ are the electrical resistance of the sensor at given concentration of VOC gas and air, respectively.

The response and recovery curves of $Co_3O_4$/CNTs@rGO sensor toward different VOCs (Ethanol, Methanol, Acetone, Toluene, and Heptane) at 50 ppm are shown in Fig. 8.

Although the higher response was noticed toward toluene but the fabricated sensor was tested toward ethanol. This is because ethanol is more widely used in different applications, and also the sensor responds rapidly to ethanol rather than toluene. In Fig. 9, the response to 50 ppm of ethanol gas is 1.36%, which is significantly higher than all of the other gases except toluene under the same concentration.

The response and recovery curves of the sensor based on $Co_3O_4$/CNTs@rGO as a function of ethanol gas concentration in the range of 10–150 ppm were investigated and represented in Fig. 10. The reproducibility of the sensor of Fig. 11 was assessed for sequential four pulses of 50 ppm ethanol, and the result indicating good reproducibility with less than 5% drift in response. The ethanol sensitivity as function of concentration is represented in Fig. 12. The obtained results demonstrated that the sensor
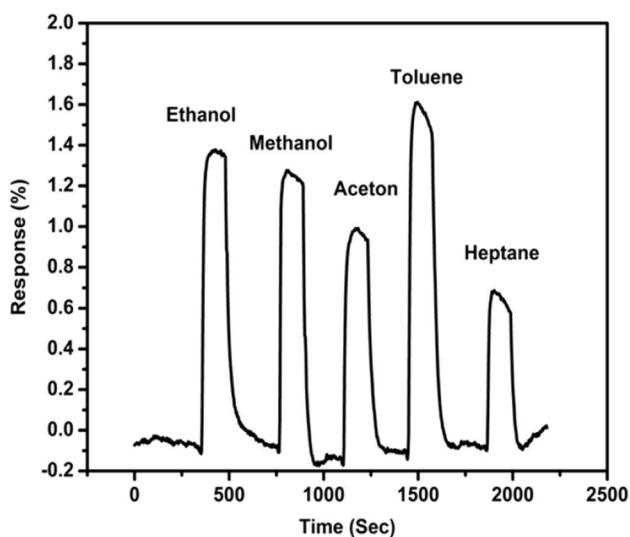
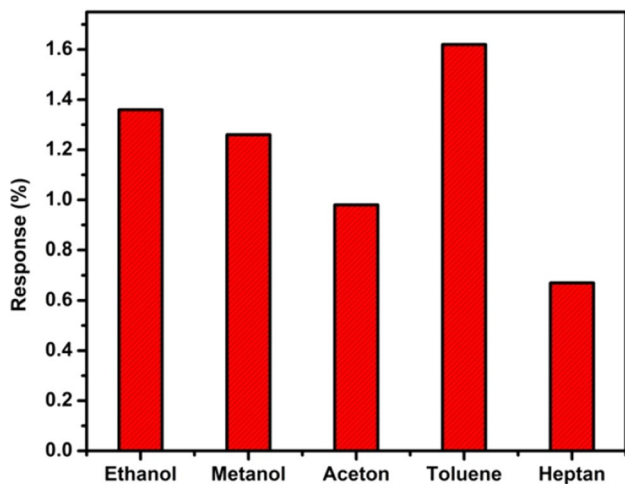**Fig. 8** Dynamic response of the Co$_3$O$_4$/CNTs@rGO sensor for VOCs



**Fig. 10** Dynamic response of the of Co$_3$O$_4$/CNTs@rGO sensor for ethanol



**Fig. 9** The comparison of the sensitivities Co$_3$O$_4$/CNTs@rGO sensor during exposure to VOCs
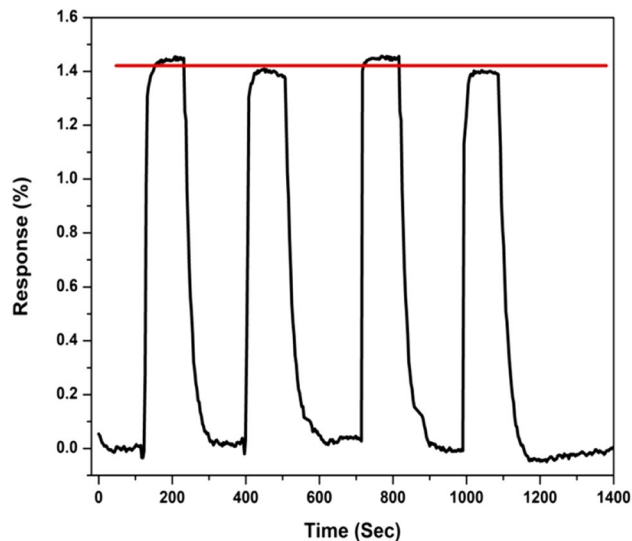


**Fig. 11** Reproducibility of the Co$_3$O$_4$/CNTs@rGO sensor at 50 ppm ethanol

instantly reacted with ethanol gas and quickly recovered afterward to its initial value after ethanol obstruction. As a p-type metal oxide semiconductor, positive holes are the main charge carriers for Co$_3$O$_4$. When gas sensors based on Co$_3$O$_4$ are tested in air, oxygen molecules are adsorbed on the surface to form negatively charged ions leading to resistance reduction of gas sensors due to the hole accumulation. However, when the sensor is subjected to reductive gas such as ethanol, the surface oxygen species react with the reductive gas, releasing the electrons back to Co$_3$O$_4$. These released electrons neutralize the holes in the Co$_3$O$_4$, and hence the resistance of gas sensors increases due to the decreased amount of positive holes.
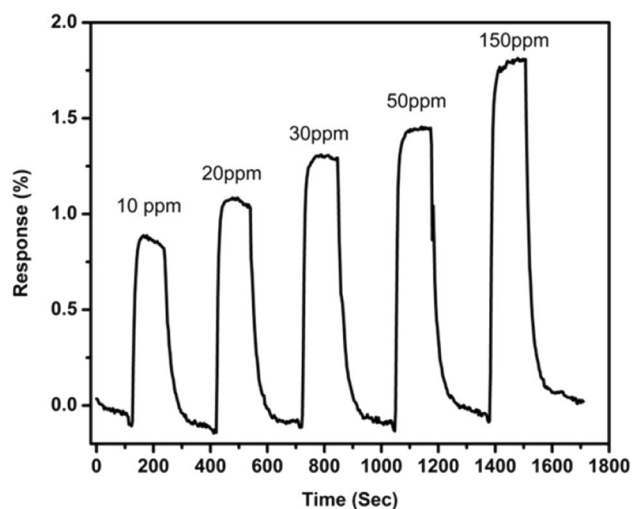
When the flow of reductive gas is interrupted, the oxygen molecules from surroundings are adsorbed on the surface of the Co$_3$O$_4$ again, and the resistance of sensors reaches its initial values. Owing to the large specific surface area and porous structure of Co$_3$O$_4$ CNTs@rGO, the ethanol gas molecules could be effortlessly diffused to the active sites at first glance and within the material through the mesoporous structure. In this work, the modified structure of Co$_3$O$_4$ CNTs@rGO can enhance the free electron exchange rate, lowering down the optimal working temperature and accelerating the diffusion of ethanol through the surface of the material.
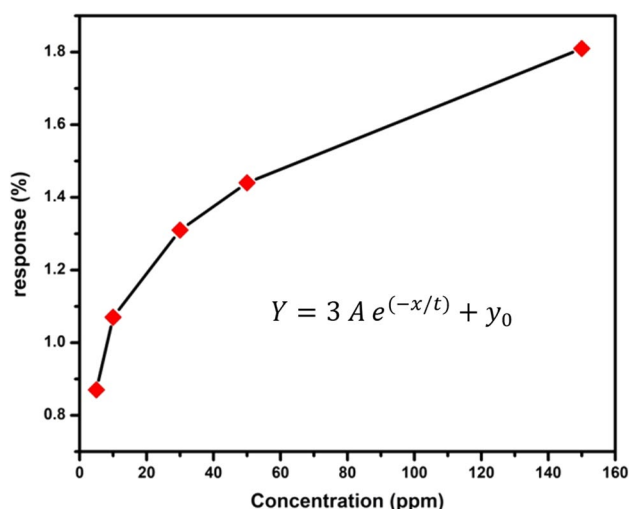
**Fig. 12** Ethanol sensitivity as function of concentration

The equation shown in the figure:

$$Y = 3\,A\,e^{(-x/t)} + y_0$$

## 5 Conclusions

Both CNTs and the rGO, were loaded with $Co_3O_4$ mesoporous nanoparticles via hydrothermal route. The HRTEM observations proved that the resultant composite contains semispherical $Co_3O_4$ particles attached to both the CNTs and the rGO surfaces. The XRD analysis indicated the formation of pure $Co_3O_4$ without any impurities. Spectroscopic techniques including Raman and FTIR assured the structure of $Co_3O_4$ with Co2+ (3d7) and Co3+ (3d6) located at tetrahedral and octahedral sites. The mesoporous structure of the resultant composite was explicated using BET and BJH measurements. The results of gas sensitivity measurements revealed that the sensor responds to VOCs at room temperature and recovers to its initial value. The response of sensor to 50 ppm of ethanol gas concentration was estimated to be 1.36%, with fast recovery time.

## References

1. S. Vetter, S. Haffer, T. Wagner, M. Tiemann, Sens. Actuators B **206**, 133 (2015)
2. M. Penza, P.J. Martin, J.T.W. Yeow, *Gas Sensing Fundamentals, Springer Series on Chemicals Sensors and Biosensors* (Springer, Berlin, Heidelberg, 2014), pp. 109–174
3. L. Zhang, X. Jing, J. Liu, J. Wang, Y. Sun, Sens. Actuators B **221**, 1492 (2015)
4. X. Qiang, M. Hu, B. Zhao, Y. Qin, T. Zhang, L. Zhou, J. Liang, Mater. Sci. Semicond. Process. **79**, 113 (2018)
5. G. Li, C. Zhang, Z. Wang, H. Huang, H. Peng, X. Li, Appl. Catal. A **550**, 67 (2018)
6. T. Zhou, T. Zhang, J. Deng, R. Zhang, Z. Lou, L. Wang, Sens. Actuators B **242**, 369 (2017)
7. S.F. Shen, M.L. Xu, D.B. Lin, H.B. Pan, Appl. Surf. Sci. **396**, 327 (2017)
8. Q. Yang, C. Feng, J. Liu, Z. Guo, Appl. Surf. Sci. **443**, 401 (2018)
9. X. Ren, H. Fan, J. Ma, C. Wang, M. Zhang, N. Zhao, Appl. Surf. Sci. **441**, 194 (2018)
10. S.A. Pawar, D.S. Patil, J.C. Shin, J. Ind. Eng. Chem. **54**, 162 (2017)
11. M. Patel, W.H. Park, A. Ray, J. Kim, J.H. Lee, Data Brief. **14**, 68 (2017)
12. K. Xu, L. Yang, J. Zou, Y. Yang, Q. Li, Y. Qu, J. Ye, C. Yuan, J. Alloy. Compd. **706**, 116 (2017)
13. S. Vladimirova, V. Krivetskiy, M. Rumyantseva, A. Gaskov, N. Mordvinova, O. Lebedev, M. Martyshov, P. Forsh, Sensors **17**, 1 (2017)
14. Y. Wang, Z. Zhao, Y. Sun, P. Li, J. Ji, Y. Chen, W. Zhang, J. Hu, Sens. Actuators B **240**, 664 (2017)
15. J. Deng, R. Zhang, L. Wang, Z. Lou, T. Zhang, Sens. Actuators B **209**, 449 (2015)
16. S. Deng, X. Liu, N. Chen, D. Deng, X. Xiao, Y. Wang, Sen. Actuators B **233**, 615 (2016)
17. J. Sasaki, M. Suzuki, K. Hanabusa, Bull. Chem. Soc. Jpn. **91**, 538 (2018)
18. Y. Wang, X. Hu, K. Zheng, X. Wei, Y. Zhao, Catal. Commun. **111**, 70 (2018)
19. X. Li, J. Wang, D. Xie, J. Xu, R. Dai, L. Xiang, H. Zhu, Y. Jiang, Sens. Actuators B **221**, 1290 (2015)
20. S.S. Varghese, S.H. Varghese, S. Swaminathan, K.K. Singh, V. Mittal, Electronics **4**, 651 (2015)
21. V. Singh, Diamond Relat. Mater. **87**, 202 (2018)
22. R. Hu, H. Zhang, Y. Bu, H. Zhang, B. Zhao, C. Yang, Electrochim. Acta **228**, 241 (2017)
23. Q. Yang, J. Wu, K. Huang, M. Lei, W. Wang, S. Tang, P. Lu, Y. Lu, J. Liu, J. Alloy. Compd. **667**, 29 (2016)
24. Z. Wen, L. Zhu, L. Mei, L. Hu, Y. Li, L. Sun, H. Cai, Z. Ye, Sens. Actuators B **186**, 172 (2013)
25. M. Morsy, M. Helal, M. El-Okr, M. Ibrahim, Spectrochim. Acta Part A **132**, 594 (2014)
26. M. Soylak, D. Acar, E. Yilmaz, S.A. El-Khodary, M. Morsy, M. Ibrahim, J. AOAC Int. **100**, 1544 (2017)
27. D. Li, Z. Chen, RSC Adv. **3**, 5003 (2013)
28. Y. Zheng, A. Wang, Z. Wang, L. Fu, F. Peng, J. Province, N.B. Garden, M.S. Yat-sen, H. Kong, J. Mater. Res. **20**, 15 (2017)
29. S. Farhadi, M. Javanmard, G. Nadri, Acta Chim. Slov. **63**, 335 (2016)
30. S. Todros, E.B. Marchi, A. Vomiero, A. Quaranta, S. Restello, G. Mariotto, G. Della Mea, Sens. Actuators B: Chem. **93**, 495 (2003)
31. M.S. Dresselhaus, A. Jorio, M. Hofmann, G. Dresselhaus, Nano Lett. **10**, 751 (2010)
32. L. Bokobza, J. Zhang, Express Polym. Lett. **6**, 601 (2012)
33. M.A. Atieh, O.Y. Bakather, B. Al-tawbini, A.A. Bukhari, F.A. Abuilaiwi, M.B. Fettouhi, Bioinorg. Chem. Appl. **2010**, 1 (2010)
34. S. Umrao, S. Abraham, F. Theil, S. Pandey, V. Ciobota, P.K. Shukla, C.J. Rupp, S. Chakraborty, R. Ahuja, J. Popp, B. Dietzek, A. Srivastava, RSC Adv. **4**, 59890 (2014)
35. B. Wang, X.-Y. Lu, K.Y. Wong, Y. Tang, Mater. Chem. Front. **1**, 468 (2017)
36. J.H. Lee, Sens. Actuators B **140**, 319 (2009)